Biophysical Journal
Article

Biophysical Society

High-Force Magnetic Tweezers with Hysteresis-Free Force Feedback

Delf Kah,[1] Christopher Dürrbeck,[1] Werner Schneider,[1] Ben Fabry,[1] and Richard Carl Gerum[1,*]
[1]Biophysics Group, Department of Physics, University of Erlangen-Nürnberg, Erlangen, Germany

ABSTRACT Magnetic tweezers based on a solenoid with an iron alloy core are widely used to apply large forces (~100 nN) onto micron-sized (~5 μm) superparamagnetic particles for mechanical manipulation or microrheological measurements at the cellular and molecular level. The precision of magnetic tweezers, however, is limited by the magnetic hysteresis of the core material, especially for time-varying force protocols. Here, we eliminate magnetic hysteresis by a feedback control of the magnetic induction, which we measure with a Hall sensor mounted to the distal end of the solenoid core. We find that the generated force depends on the induction according to a power-law relationship and on the bead-tip distance according to a stretched exponential relationship. Combined, they describe with only three parameters the induction-force-distance relationship, enabling accurate force calibration and force feedback. We apply our method to measure the force dependence of the viscoelastic and plastic properties of fibroblasts using a protocol with stepwise increasing and decreasing forces. We group the measured cells in a soft and a stiff cohort and find that softer cells show an increasing stiffness but decreasing plasticity with higher forces, indicating a pronounced stress stiffening of the cytoskeleton. By contrast, stiffer cells show no stress stiffening but an increasing plasticity with higher forces. These findings indicate profound differences between soft and stiff cells regarding their protection mechanisms against external mechanical stress. In summary, our method increases the precision, simplifies the handling, and extends the applicability of magnetic tweezers.

SIGNIFICANCE Magnetic tweezers are widely used, versatile tools, e.g., for investigating the mechanical behavior of cells and for measuring the strength of receptor-ligand bonds. A limitation of existing magnetic tweezer setups, however, is caused by the magnetic hysteresis of the tweezer core material. Magnetic hysteresis considerably complicates protocols in which the forces decrease over time and moreover requires that the tweezer core must be demagnetized (de-Gaussed) before each measurement. We describe how these limitations can be overcome with a force feedback through direct magnetic field measurement. We demonstrate the applicability of our setup by investigating the force-dependent viscoelastic and plastic deformations of fibroblasts.

INTRODUCTION

Magnetic tweezers are widely used tools for manipulation, force measurements, and force application at the cellular and molecular level (1). Magnetic tweezers have been applied for cell rheology measurements (2), for investigating the binding strengths of specific membrane proteins (3), or for manipulating individual DNA molecules (4). Their force range is typically on the order of 10^{-3}–10^{4} pN (5), surpassing optical tweezers (6) and dielectrophoresis-based tweezers (7) by several orders of magnitude.

The simplest design for magnetic tweezers is an electromagnet in the form of a solenoid with a core made from a material with high magnetic permeability, such as iron alloys. The core is tapered to a sharp tip on one side with a radius of usually less than 10 μm. At the tip, a high gradient magnetic field is formed, which attracts nearby superparamagnetic beads (8). A major drawback, however, is the effect of magnetic hysteresis of the core material, which is caused by remanent magnetization (9–12). Magnetic hysteresis implies that the magnetization of the core material does not only depend on this solenoid current but also on its history. Practically, this means that the relationship between solenoid current and the generated force is difficult to predict and is usually calibrated only for a single, specific current protocol, e.g., for increasing currents after core demagnetization (de-Gaussing). Thus, the remanent magnetization of

Submitted December 2, 2019, and accepted for publication May 20, 2020.
*Correspondence: richard.gerum@fau.de
Delf Kah and Christopher Dürrbeck contributed equally to this work.
Editor: Philip LeDuc.
https://doi.org/10.1016/j.bpj.2020.05.018

the solenoid core must be eliminated after each measurement by applying a sinusoidally alternating solenoid current with decreasing amplitude (8,13). However, de-Gaussing always causes a large, sudden, distance-dependent application of force to nearby beads, even when performed very quickly. Alternatively, a smaller current in the opposite direction can be applied to compensate for the remanent magnetic field of the core, but the magnitude of this countercurrent needs to be specifically calibrated for each force protocol (14). Another common strategy to mitigate the problems associated with magnetic hysteresis is to use a core made from Mu-metal, a nickel-iron-molybdenum alloy optimized for low hysteresis. However, Mu-metal has a considerably lower maximal magnetic induction compared to conventional iron alloys (15,16) and can regain hysteretic behavior after machining, e.g., after sharpening the tip with a grinder.

It is also possible to eliminate the high-permeability core altogether and to generate the magnetic field and the field gradient with a pair of coaxial coils of opposite polarity (17). In contrast to conventional magnetic tweezers, this system greatly simplifies the control of the magnetic force but is unsuitable for many biophysical applications because of its low maximal force of ~2 pN for 4.5-μm diameter beads.

Finally, the remanent magnetic field of the core material can be compensated by a feedback circuit to control the magnetic induction instead of the magnetic current. Such a system has previously been employed in a four-pole tweezer setup (18). There, the primary function of the induction feedback was the reduction of magnetic cross-talk among the solenoids but not the compensation for the hysteresis of the core material. The maximal force of this setup was ~1 pN for 2.8-μm diameter beads, which is too low for many applications.

In this study, we present a high-force single-pole magnetic tweezer setup with induction feedback based on a Hall probe. By compensating the magnetic hysteresis of the core material, we can apply arbitrary force protocols with an amplitude of up to 100 nN to 5-μm diameter superparamagnetic beads. We also provide an empirical equation with only three free parameters to describe the applied force as a function of the bead-needle distance and the magnetic induction for different superparamagnetic beads and for different core materials. This equation can be incorporated into the feedback loop to perform controlled-force experiments. To illustrate the versatility of this tweezer setup for cell biology studies, we apply increasing and decreasing force steps to murine embryonic NIH-3T3 fibroblasts to measure the nonlinear (force-dependent) viscoelastic and plastic cell rheology.

MATERIALS AND METHODS

System design

The magnetic tweezer core is a 100-mm-long cylinder with a diameter of 4.5 mm, made of either St37 steel or Mu-metal (Vacuumschmelze, Hanau, Germany) (Fig. 1, *a–c*). While the cylinder is continuously turned by a milling machine (Fig. 1 *c*, *inset*), one end of the cylinder is tapered with a precision drill grinder to a sharp tip with an opening angle of 60° and a tip radius <5 μm (for details, see (19)). In the following, we refer to the sharpened tweezer core as the needle.

A Hall sensor (SS495A; Honeywell, Charlotte, NC) for measuring the magnetic induction is mounted at the rear (blunt) end of the needle. The needle is inserted in a solenoid with ~200 windings (24-gauge copper wire) on a brass body. The solenoid current is supplied by a high-current operational amplifier (OPA549T; Texas Instruments, Dallas, TX).

The needle is attached to a micromanipulator (InjectMan NI2; Eppendorf, Hamburg, Germany) to allow for precise movements of the needle tip. The position of the needle tip relative to a magnetic bead (for example, a bead that is attached to a cell or suspended in oil) is measured with an inverted bright field microscope equipped with a 40×, 0.6 NA long working distance objective (Leica, Wetzlar, Germany). A specially manufactured nonmagnetic objective is used because conventional objectives with nickel/chrome housings can distort the magnetic field in the object plane (20). Images are taken with a CCD camera (Orca-spark; Hamamatsu Photonics, Hamamatsu, Japan), which is triggered by a data acquisition card (NI-6052E; National Instruments, Austin, TX), typically at a rate of 50 frames/s. The analog output of the data acquisition card provides the set point of the magnetic induction for the feedback-loop circuit that is described below. In this way, image acquisition can be synchronized to the force protocol. This synchronization is particularly important when recording fast movements of beads after sudden changes in force.

To achieve a high frame rate, only a region of interest of 1920 × 128 pixels is recorded during the measurement, which corresponds to a field of view of 310 × 21 μm. This resolution is sufficient to extract the bead-tip distance and the bead trajectory. Images are transferred to a computer via a USB 3.0 connection and evaluated with software written in Python (21), which utilizes the Micromanager framework (22). The beads are tracked with an intensity-weighted center-of-mass algorithm (23). The position of the needle tip is determined in a process of thresholding, erosion, and dilation operations, which yields a binary image of needle and background. For each acquired frame, the bead position, the bead-to-tip distance, and the solenoid current are stored in an SQLite database file.

Design of the control loop

The centerpiece of the control loop is a high-current operational amplifier, which is operated as a noninverted amplifier. The target voltage of the amplifier (at the noninverted input) is provided by a data acquisition card. The feedback voltage (at the inverted input of the amplifier) is the amplified and phase-compensated magnetic induction signal measured by the Hall sensor. The amplifier output is connected to the solenoid. Positive feedback from high-frequency sources is suppressed with a 100 nF capacitor placed between the output and the inverted input of the amplifier (Fig. 1 *a*).

The Hall sensor is a ratiometric linear sensor, which is operated with a stabilized input voltage of 10 V from a voltage reference circuit (AD587; Analog Devices, Norwood, MA). The measuring range of the Hall sensor is −67 to 67 mT. At the zero magnetic field, the output voltage of the sensor is half the operating voltage, i.e., 5 V. This offset is removed with a resistor network in combination with an instrumentation amplifier (INA114AP; Texas Instruments) with unity gain.

The 1 kΩ potentiometer of the resistor network is used to adjust the zero-force point for a zero induction input voltage as follows: superparamagnetic beads with a radius of 5.09 μm (microParticles, Berlin, Germany) are suspended in water at a concentration of 5×10^6 particles/mL, and the magnetic tweezer needle is briefly magnetized to attract beads. The potentiometer of the resistor network is then adjusted until the beads detach from the needle tip when the microscope stage is abruptly moved.

Because the Hall probe has a response time of 3 ms, a phase-compensation RC filter is needed to suppress positive feedback, which can give rise to

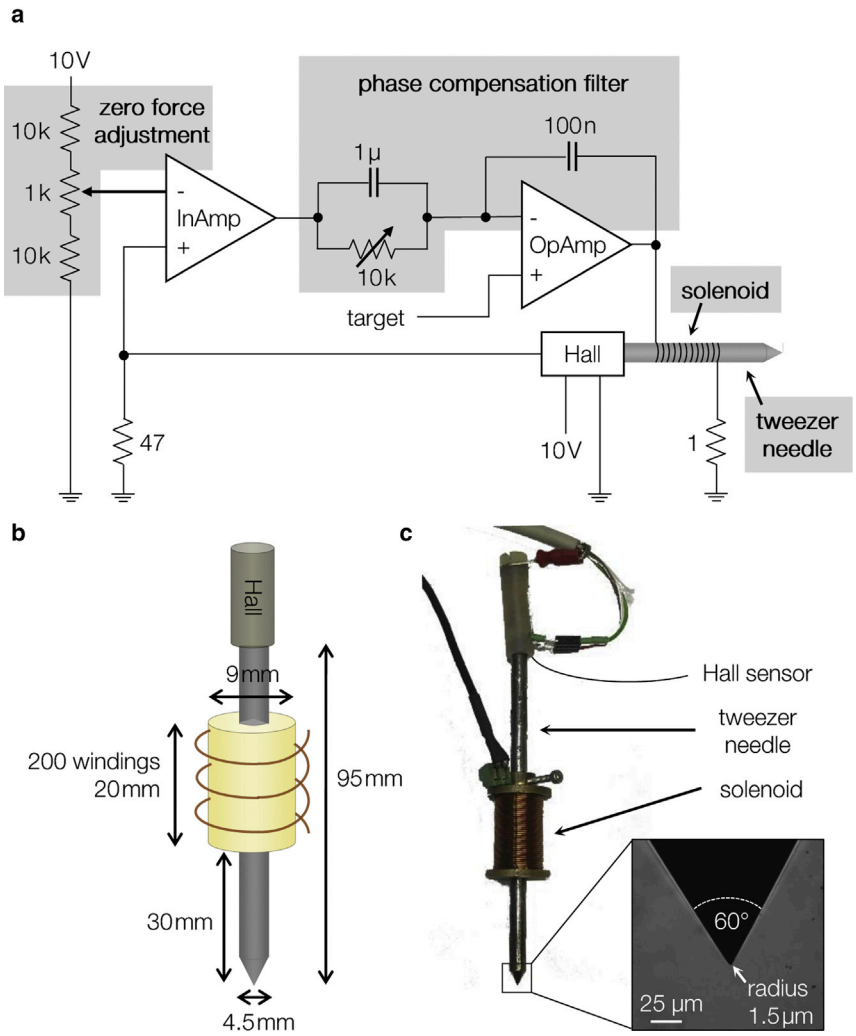

FIGURE 1 Electronic circuit and tweezer design. (*a*) The feedback control loop consists of three main components: a Hall probe for a continuous measurement of the magnetic induction, an instrumentation amplifier to process the Hall signal, and a high-voltage/high-current operational amplifier to control the solenoid current. The operational amplifier compares the target value to the value measured by the Hall sensor. Through the feedback loop, the operational amplifier adjusts the solenoid current, until the measured value from the Hall probe equals the target value. Zero force can be adjusted with a potentiometer. (*b* and *c*) The magnetic tweezer needle is magnetized by a solenoid (200 windings). The generated magnetic field is sensed by a Hall probe that is mounted to the rear end of the magnetic tweezer needle. The needle has a sharp tip with an opening angle of 60° and a radius of 1.5 μm to generate a high magnetic field gradient. To see this figure in color, go online.

high-frequency (>1 kHz) current oscillations. The 10 kΩ potentiometer of the RC filter is adjusted to minimize response time, current overshoot, and current oscillations when a square-wave signal of 1 V and 10 Hz is applied as the target signal (Fig. 2 *c*).

Validation of hysteresis compensation

We first recorded the hysteresis of the needle material (St37 steel) with the magnetic feedback turned off. For this purpose, we applied a triangular current protocol with a period time of 12 s and an amplitude of 2 A (Fig. 2 *a*, inset) and measured the magnetic induction with a Hall probe (Fig. 2 *a*). As expected, we found a nonlinear relationship between the magnetic field and the magnetic induction and a pronounced hysteresis effect (remanent magnetization of 1.8 mT). With the magnetic feedback turned on, we recorded a linear response between target and measured magnetic induction with an average deviation (root mean-square) of 18 μT that was free of hysteresis (Fig. 2 *b*).

To characterize the dynamic response of the control loop, we recorded the coil current and the magnetic induction in response to a square-wave target signal (1 V, 10 Hz) (Fig. 2 *c*). The induction, as measured with the Hall probe, approached the target value within 3 ms with a small overshoot of less than 10% but without noticeable oscillations. The coil current displayed a larger overshoot during the first 3 ms after a sudden change in the target induction. The overshoot reflects the energy needed to overcome the hysteretic behavior of the needle and is to some degree a consequence of the finite response time of the Hall probe.

Force calibration

The force that is exerted by the magnetic tweezers on a bead depends on the properties of both the bead and the needle. Influencing factors include the radius of the bead, its susceptibility, the volume fraction of magnetic nanoparticles, the susceptibility of the needle core material, and the geometry of the tip. Most importantly, the force exerted on a bead depends nonlinearly on the solenoid current (or the magnetic induction) and the distance between bead and needle tip (14).

We calibrated the induction-distance-force relationship of the tweezer system as described below. Note that during force calibration, the hysteresis compensation must always be active, regardless of the core material. We compared two types of superparamagnetic beads with different iron contents and functionalizations, namely 1) epoxylated beads with a diameter of 4.5 μm and 20% iron oxide content (Dynabeads M-450; Invitrogen, Carlsbad, CA) and 2) carboxylated beads with a diameter of 5.09 μm and 80% iron oxide content (microParticles). In the following, these two types of beads are abbreviated as *Fe20* and *Fe80*, respectively. For a calibration measurement, the beads are suspended in a viscous liquid of known viscosity (poly-dimethylsiloxane (PDMS) oil (Sigma-Aldrich, St. Louis, MO) with a dynamic viscosity of 9.65 or 28.95 Pa $\times$ s) and filled into a glass

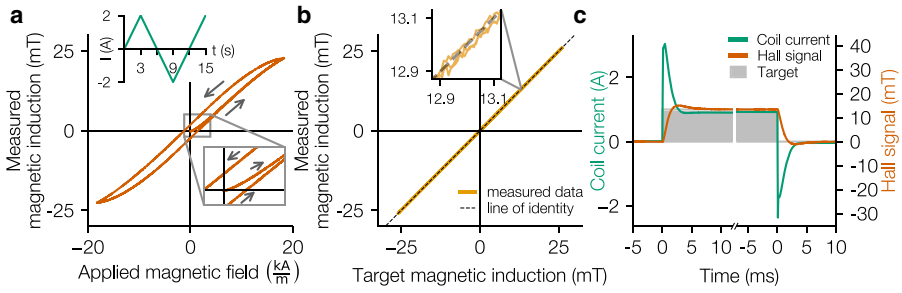

FIGURE 2 Hysteresis compensation and high-frequency response of the control loop. (*a*) Magnetization curve of a ST37 tweezer needle measured with a Hall probe in response to a triangular current protocol (current protocol shown in *inset*). (*b*) Magnetic induction was measured with a Hall probe versus target induction for a triangular protocol when the induction feedback loop is turned on. Dashed line shows the line of identity. Inset shows the noise level of 18 μT. (*c*) Step response of the control loop (induction measured with Hall probe (*orange*) and solenoid current (*green*) for a square-wave target signal (*gray*)). The sampling rate was 10^3 Hz in (*a*) and (*b*) and 10^5 Hz in (*c*). To see this figure in color, go online.

dish (cf. Supporting Materials and Methods, Section S1 for a detailed protocol of the experiment). The glass dish is moved with a manual microscope stage so as to position a single bead 50 μm in front of the needle tip. Next, a square-wave magnetic induction is applied in an 1 s on/1 s off sequence until the bead has reached the tip. Subsequently, another bead is selected, positioned 50 μm in front of the needle tip, and the procedure is repeated with different amplitudes of the magnetic induction in a range between 1.3 and 20.8 mT.

The beads perform a stop-and-go-like motion in response to the square-wave pattern of the magnetic induction. Occasionally, bead movements occur during the off-phase because of convective drift in the PDMS oil after positioning the bead in front of the needle. If such bead movement is observed, the measurement is discarded. The force acting on the bead is then calculated using Stoke's law from the speed of bead movements during the on-phase:

$$F(B,d) = 6\pi \cdot r \cdot \eta \cdot v(B,d), \tag{1}$$

where r is the radius of the bead, η is the viscosity of the oil, and v is the bead velocity for a given bead-needle distance d and magnetic induction B. The measured force versus bead-needle distance relationship (Fig. 3) followed a stretched exponential function,

$$F(B,d) = \alpha(B) \cdot \exp\left(- \left(\frac{d}{d_0} \right)^{\beta(B)} \right). \tag{2}$$

The factors α and β both depend on the magnetic induction B. The bead-needle distance d in Eq. 2 is given in units of μm, and the normalization of d with an arbitrary value of $d_0 = 1$ μm is introduced to remove the physical units for consistency.

The prefactor α increased with increasing B according to a power law,

$$\alpha(B) = p_1 \cdot \left(\frac{B}{B_0} \right)^{p_2}, \tag{3}$$

with calibration parameters p_1 and p_2. The magnetic induction B is given in units of mT. The normalization of B with with an arbitrary value of $B_0 = 1$ mT in Eq. 3 is introduced to remove the physical units for consistency.

Interestingly, we discovered that the factor α to the power of β is constant for all values of the magnetic induction:

$$\alpha(B)^{\beta(B)} = p_3, \tag{4}$$

with p_3 being the third calibration parameter. Taken together, Eqs. 2, 3, and 4 describe the force F as a function of magnetic induction B and the bead-needle distance d with only three fit parameters.

The values of the fit parameters p_1, p_2, and p_3 depend on the combination of bead type and needle material as shown in Table 1. Accordingly, the combination of Fe80 beads (high iron content and thus high magnetic dipole moment) and St37 core material (high magnetic induction) resulted in the highest forces. The fit parameters were determined from the data shown in Fig. 3 by a least-squares fit. Alternatively, we determined the fit parameters as well as their confidence intervals using the Markov chain Monte Carlo method and found that the resulting parameters deviate by a maximum of 2% from those given in Table 1 (Supporting Materials and Methods, Section S6).

To implement a magnetic tweezer system with force feedback for situations in which the beads are moving, Eqs. 2, 3, and 4 can be numerically inverted to compute in real time the magnetic induction B necessary to exert a defined force. In our system, the response time of the force feedback control is determined by the the camera frame rate of 50 Hz (corresponding to a delay of 20 ms), the computation time of ~12 ms for determining the bead-needle distance from the image frames, and the response time of the electronic feedback loop of less than 3 ms (Fig. 2 *c*).

Cell culture and sample preparation

We conducted microrheological experiments on NIH-3T3 murine embryonic fibroblasts. 50,000 cells were harvested with 0.25% trypsin-EDTA (Gibco, Thermo Fisher Scientific, Waltham, MA) and seeded in 35-mm plastic dishes treated for tissue culture (Nunc; Thermo Fisher Scientific). Cells were grown overnight in high-glucose Dulbecco's modified Eagle's medium with 10% bovine calf serum (Sigma-Aldrich), 1% penicillin and streptomycin (#15140122; Gibco), 1 mM sodium pyruvate, and 4 mM L-glutamine. Superparamagnetic Fe80 beads with a diameter of 5.09 μm were coated with the extracellular matrix protein fibronectin (FN) (50 μg/mL in PBS overnight at 4°C) (24). FN was chosen because it strongly binds to transmembrane receptors and establishes a tight mechanical linkage between the microbead and the cytoskeleton (25). FN-coated beads were sonicated for 15 s, added to the cell culture dish at a 2:1 bead/cell ratio, and incubated at 5% CO_2 at 37°C. After 30 min, the cell medium was changed to wash-off unbound beads. Measurements were performed at room temperature for a maximal duration of 30 min. Between individual cell measurements, the dish was moved by at least 200 μm to ensure that the cell being measured had not been exposed to significant forces during preceding measurements.

RESULTS

Force feedback

To demonstrate the combined performance and accuracy of the force calibration, hysteresis compensation, and force

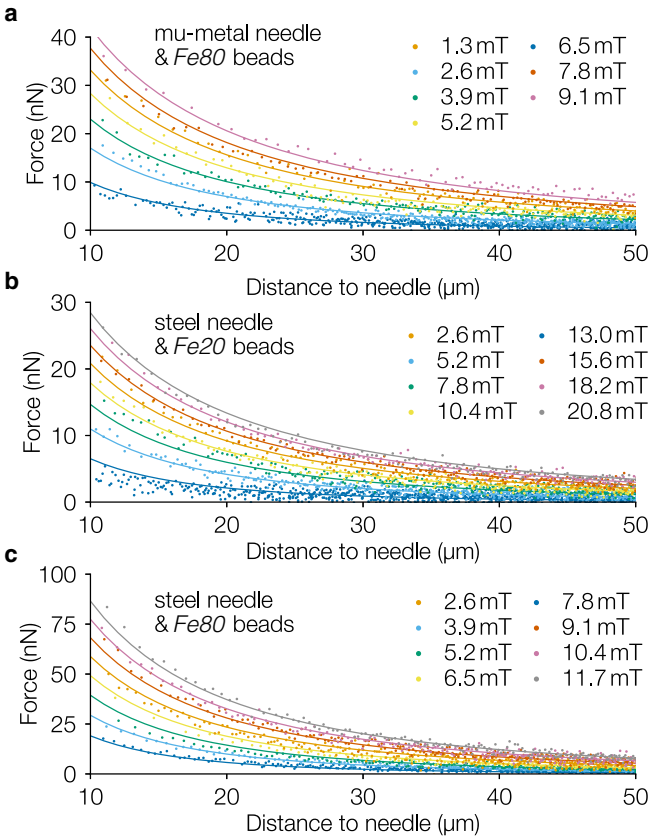

FIGURE 3 Force calibration. Force-distance curves for different magnetic inductions and for different combinations of tweezer needle material and superparamagnetic beads. The hysteresis compensation is activated for all cases. (*a*) Mu-metal needle with carboxylated Fe80 beads, (*b*) steel needle with epoxylated Fe20 beads, and (*c*) steel needle with carboxylated Fe80 beads. Solid lines indicate the fits with a stretched exponential function with three parameters (Eqs. 2, 3, and 4). To see this figure in color, go online.

feedback components of our system, we applied increasing and decreasing force steps (target force) to beads suspended in a viscous medium and measured the actual forces from the speed of the bead's movements using Eq. 1. Specifically, we suspended superparamagnetic beads with a diameter of 5.09 μm (Fe80) in PDMS oil with a dynamic viscosity of 28.95 Pa $\times$ s and positioned each bead to be measured at a distance of $\sim$60 μm from the de-Gaussed needle tip (St37). The target force protocol consisted of five increasing discrete steps (1, 2, 4, 8, and 16 nN) starting from zero force, followed by five decreasing discrete steps (8, 4, 2, 1, and 0 nN) (see Fig. 4 *a*). Each step lasted 1 s. During force application, the bead moved by a distance of around 30 μm toward the needle tip (*blue line* in Fig. 4 *a*). From the momentary speed of the bead, we calculated the momentary forces acting on the bead (*orange points* in Fig. 4 *a*) and the median forces during the duration of the force plateau (*black line* in Fig. 4 *a*) and compared them to the target forces (*gray area*).

TABLE 1 Calibration Parameters for Different Combinations of Bead and Core Materials

Core Material	Bead	p_1	p_2	p_3	Force[a]
St37	Fe20	78.5 nN	0.47	9.5	17 nN
Mu-metal	Fe80	143.6 nN	0.52	10.0	45 nN
St37	Fe80	201.8 nN	0.70	17.8	75 nN

[a]The forces are computed for a distance of 10 μm and a magnetic induction of 10 mT.

The relationship between measured and target forces was close to the line of identity for ascending force steps, with a coefficient of determination of $R^2 = 0.950$ (Fig. 4 *b*), demonstrating both the accuracy of the calibration and force feedback. Importantly, we found a similarly high coefficient of determination of $R^2 = 0.949$ for descending force steps, demonstrating the quality of the hysteresis compensation. The force measured at the end of the protocol with a target force of zero was slightly increased to 0.23 $\pm$ 0.12

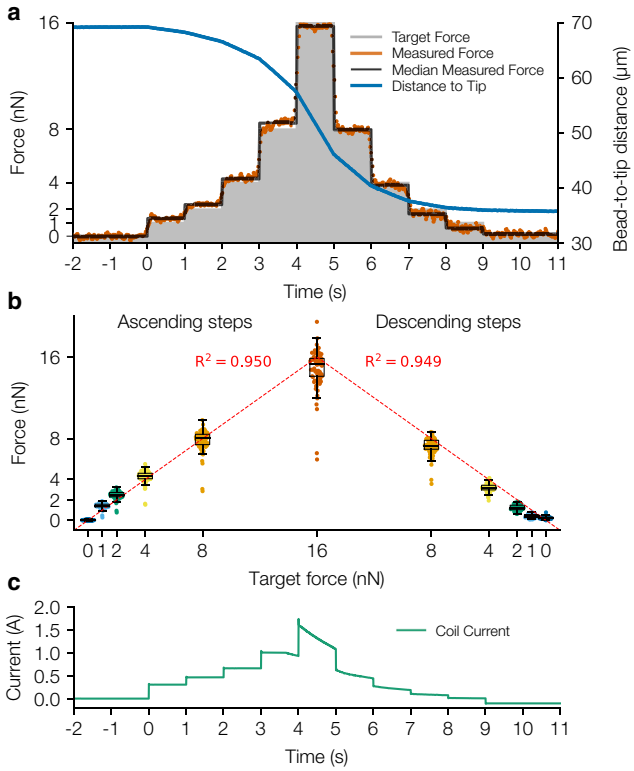

FIGURE 4 Test with pyramidal force steps. (*a*) Example of a bead trajectory (*blue*) in response to a step-force protocol (target force is indicated by the *gray shaded area*) for a superparamagnetic bead in PDMS oil (dynamic viscosity of 28.95 Pa $\times$ s). The force (momentary force shown in *orange*, median force over 1 s shown in *black*) was calculated from the measured bead trajectory. (*b*) Forces measured during ascending and descending force steps versus target forces. Points represent measurements performed on individual beads (n = 81), and boxplots indicate median values, lower to upper quartile values, and 1.5 interquartile ranges. The line of identity (*dashed red line*) describes the relationship between measured forces and target forces with a coefficient of determination of $R^2 = 0.950$ for ascending forces and 0.949 for descending forces. (*c*) Coil current versus time. To see this figure in color, go online.

nN (n = 81 beads) compared to 0.01 ± 0.04 nN at the beginning of the protocol. Note, however, that the beads were considerably closer to the needle tip at the end of the protocol (30 ± 9 μm on average; mean ± SD) than at the beginning (61 ± 7 μm on average). Given the exponential relationship between force and bead-to-tip distance (Eq. 2), even a small remanent field can cause measurable forces. In addition, numerous beads tended to accumulate at the needle tip during force application, which distorts the magnetic field and field gradient. The latter effect should not be a problem when measuring cells as unbound beads are washed off before starting the experiment.

The coil current (Fig. 4 *c*) increased with higher target forces and decreased over time during the application of a constant force as the bead approached the needle tip (*blue line* in Fig. 4 *a*). Note that the coil current during the zero-force phase at the beginning was almost zero as the needle had been freshly de-Gaussed. During the zero-force phase at the end, by contrast, the coil current was negative to compensate for the remanent magnetic field of the needle (Fig. 4 *c*).

Viscoeleastic and plastic behavior of fibroblasts

To measure the viscoeleastic and plastic behavior of fibroblasts, the force was increased from 1 to 16 nN in steps of 3-s duration with plateau values of 1, 2, 4, 8, and 16 nN. Subsequently, the force was decreased in the same pattern, resulting in pyramidal force steps (*gray bars* in Fig. 5 *a*). The bead position was monitored for 5 s before force application (initial phase) and for 10 s after force application (relaxation phase).

The deformation of living cells in response to a step-like force typically followed a power law in time (26,27). After force removal, the cells tended to return to their original shape, also following a power law in time (26). The shape recovery was usually incomplete because of irreversible plastic deformations (24).

The displacement $d(t)$ of the cell in response to a single force-on step can be described by a power law with exponent β and a factor $(a + s)$, where a is the viscoelastic compliance and s is the plastic compliance (upper part of Eq. 5):

Here, $(t - t_{on})$ is the time that has passed since a force has been applied at $t = t_{on}$, t_{1s} is a consistency factor of 1 s (an arbitrary choice), t_{off} is the time point when the (upward) force step is completed (and the downward force step is started), and ΔF is the amplitude of the force step. The sum of $a + s$ represents the total compliance, which corresponds to the displacement of a bead after 1 s of force application, normalized to the force amplitude. Upon force removal, the viscoelastic part of the cell's deformation is reversible and returns gradually to zero (first part of the lower part of Eq. 5), whereas the plastic part of the deformation remains constant (second part of the lower part of Eq. 5).

Pyramidal force steps can be described by the superposition of multiple force plateaus, and the resulting bead displacement is therefore the superposition of bead displacements in response to each individual force step (24,26) (see Supporting Materials and Methods, Section S2 for details on the mathematical description). For increasing forces, both the viscoelastic and plastic components of Eq. 5 contribute to the bead displacement toward the needle tip. By contrast, for decreasing forces, only the viscoelastic component contributes to the bead recoil away from the needle tip, whereas the bead displacements resulting from the plastic deformation of past force steps are frozen in time.

Relative plasticity of fibroblasts depends on their low-force stiffness

In previous studies, protocols with increasing force steps have been used to investigate the force-dependent stiffening of cells (3,28). These studies demonstrated a stiffening of adherent cells that was proportional to the sum of the contractile prestress and the external stress from the magnetic beads. Accordingly, cells with a high contractile prestress that were stiff at low forces showed less relative stiffening with increasing forces compared to soft cells. By contrast, it remains unknown how cell plasticity changes with force because plasticity can only be measured using protocols with decreasing forces that have so far been impossible because of the magnetic hysteresis of the tweezer core material. It is also unclear if the plasticity of soft and stiff cells responds differently to force.

$$d(t) = \begin{cases} (a+s)\cdot\Delta F\cdot\left(\dfrac{t-t_{on}}{t_{1s}}\right)^{\beta} & \text{if } t_{on} < t \le t_{off} \\ a\cdot\Delta F\cdot\left[\left(\dfrac{t-t_{on}}{t_{1s}}\right)^{\beta} - \left(\dfrac{t-t_{off}}{t_{1s}}\right)^{\beta}\right] + s\cdot\Delta F\cdot\left(\dfrac{t_{off}-t_{on}}{t_{1s}}\right)^{\beta} & \text{if } t_{off} < t \end{cases} . \quad (5)$$

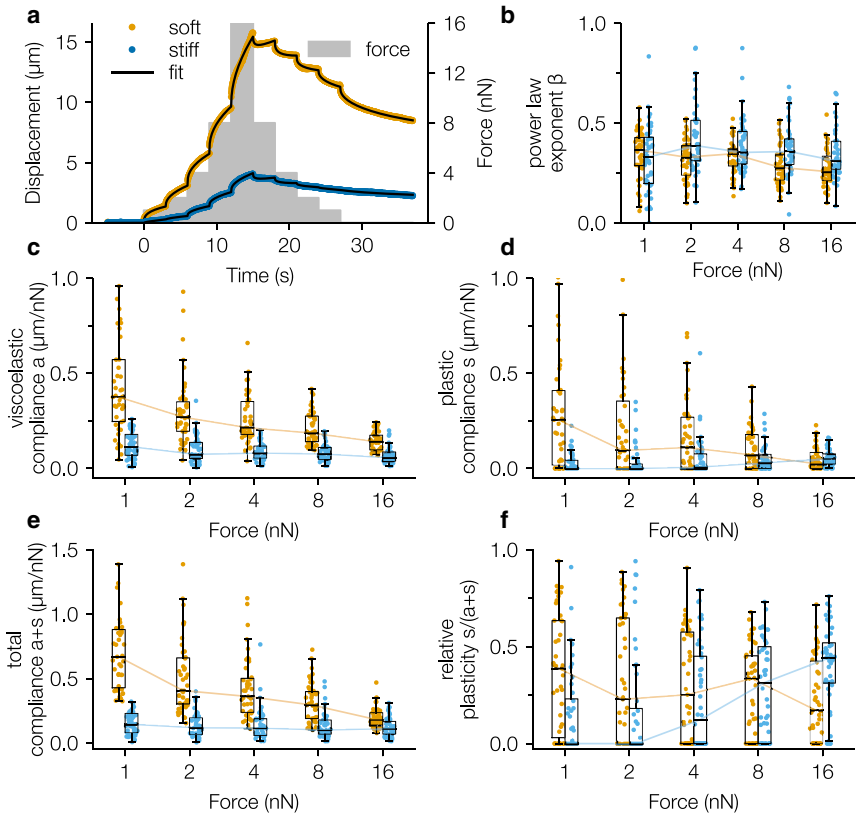

FIGURE 5 Force dependency of viscoelastic and plastic cell behavior. (*a*) Response of a representative cell with high compliance ("soft": *orange dots*) and a cell with low compliance ("stiff": *blue dots*) to pyramidal force steps (*area shaded gray*, 1, 2, 4, 8, and 16 nN) fitted with Eq. 5 (*black lines*). (*b*) power-law exponent β, (*c*) absolute viscoelastic compliance a, (*d*) absolute plastic compliance s, (*e*) total compliance $a + s$, and (*f*) relative plastic compliance s/(a + s). Data (median, 25%/75% percentiles, 1.5 interquantile range) from soft (*orange bars/lines*, n = 43 cells) and stiff (*blue bars/lines*, n = 44 cells) fibroblasts are shown as a function of force. To see this figure in color, go online.

To address these questions, we grouped the NIH-3T3 fibroblasts into a stiff and a soft cohort (1). A cell was considered "soft" if its total compliance measured at 1 nN was larger than the median of the 1 nN compliance of all cells (Fig. S3 *a*). Otherwise, the cell was considered "stiff." Measurements from individual fibroblasts were included in the subsequent analysis only if the fit of Eq. 5 to the data showed a high coefficient of determination ($R^2 > 0.991$) and a low error (square root of the 98% percentile of the squared error <0.23 μm); otherwise, the measurement was excluded. Figs. S4.1–S4.3 show the measurements and fits from all fibroblasts, both included and excluded.

From the fit of Eq. 5 to the data, we obtained for each cell and each increasing or decreasing force step a value for the viscoelastic (Fig. 5 *c*) and plastic compliance (Fig. 5 *d*) and a value for the power-law exponent β (Fig. 5 *b*). Although the power-law exponent β (Fig. 5 *b*) remained approximately constant at around 0.34 ± 0.01 (mean ± SE) for all forces for both soft and stiff cells, the viscoelastic and plastic compliance decreased strongly with force for soft fibroblasts. Stiff fibroblasts, by contrast, showed only a slight decrease in their viscoelastic compliance and a slight increase in plastic compliance. The total compliance of the stiff cohort was 0.11 ± 0.01 μm/nN at a force of 1 nN and remained almost constant for increasing force amplitudes (Fig. 5 *e*). The total compliance of the soft cohort, by contrast, decreased strongly from 0.67 ± 0.02 μm/nN at a force of 1 nN to 0.18 ± 0.01 μm/nN at a force of 16 nN (median ± standard error of the median). These observations of pronounced stress stiffening in soft cells but not in stiff cells are consistent with previous findings (28).

The plasticity of soft cells showed a similar trend as the viscoelastic compliance and decreased with increasing force (Fig. 5 *d*). By contrast, the plasticity of stiff cells increased slightly with force. At the highest force of 16 nN, the plasticity of soft and stiff cells was similar. These opposing trends of plastic cell deformations in soft versus stiff cells are also seen in the force responses of the relative plasticity (the ratio $s/(a + s)$) (Fig. 5 *f*). Together, these data indicate that stiff cells are protected from plastic deformation at low forces, whereas softer cells are protected from plastic deformation at high forces. Interestingly, the plasticity of all cells (soft or stiff), when plotted versus the total cell deformation, showed a biphasic response of low plasticity at small and large cell deformations and high plasticity at intermediate cell deformations (Fig. S7).

DISCUSSION

In this study, we present a hysteresis-free magnetic tweezer setup for applying arbitrary force protocols with a maximal force of up to 100 nN. In this setup, the magnetic induction of the tweezer core is measured with a Hall probe and is electronically feedback controlled, which eliminates any

magnetic hysteresis. It is therefore no longer necessary to de-Gauss the tweezer needle between measurements. An analytical equation with only three parameters can describe the relationship between force, magnetic induction, and bead-tip distance. Previously, five fit parameters were necessary to describe the relationship for magnetic tweezers with current feedback (14).

The volume fraction of iron oxide contained in individual beads largely determines the precision with which forces can be applied. During test measurements shown in Fig. 4 *b*, we found that beads were either consistently stronger or consistently weaker than the average at each of the target forces. For Fe20 beads, the coefficient of variation in the forces among individual beads was 14% for the highest force level of 16 nN, which is lower than the value of 18–28% reported in (14) for beads from the same manufacturer, which might indicate batch-to-batch variability. Note that the coefficient of variation cannot be reduced by increasing the calibration accuracy or by improving the force feedback but only by choosing beads with a more uniform iron oxide content.

Most importantly, hysteresis-free magnetic tweezers allow for the application of arbitrary force protocols, including protocols with descending forces. Moreover, it is no longer necessary to choose a tweezer core material with low magnetic hysteresis such as Mu-metal alloy that typically comes with a lower saturation magnetization (see Supporting Materials and Methods, Section S5) and hence lower maximal force compared to iron alloys. Also, Mu-metal regains hysteretic behavior when machined or polished, e.g., when sharpening the tweezer tip (Supporting Materials and Methods, Section S5).

We demonstrated the function and versatility of our setup by applying pyramidal force steps to superparamagnetic beads that were bound to fibroblasts. Such a protocol of ascending and descending pyramidal force steps is suitable for measuring the force dependence of the total cell compliance, i.e., the inverse of the cell stiffness. We grouped the fibroblasts into a soft and stiff cohort based on their viscoelastic response to small forces (1 nN) and found, in agreement with previous reports, that only soft cells become stiffer with increasing external forces (1). This result is consistent with the notion that cells behave like a stress-stiffening material, with the total stress being the sum of the internal contractile stress within the cytoskeleton (the so-called prestress) and the external stress applied via magnetic beads. Stiff cells have a high prestress, and the externally applied magnetic force increases the total stress only by a small fraction. Consequently, these cells do not stiffen further (28,29). In soft cells, by contrast, the total stress within the cytoskeleton is dominated by the externally applied magnetic forces. Accordingly, soft cells show pronounced stress stiffening.

By applying pyramidal force steps, we can decompose the total compliance into its viscoelastic and plastic components. Similar to the total compliance, we found that the viscoelastic compliance of the softer cell cohort decreased with force, whereas the viscoelastic compliance in the stiff cohort remained approximately constant for all forces. In soft cells, the plasticity followed the behavior of the viscoelastic compliance; it was high at low forces and steadily decreased with force. By contrast, the plasticity of stiff cells was nearly zero for low force and increased with force.

It has previously been shown that cell plasticity originates from the rupture of bonds within the cytoskeleton. Therefore, it can be expected that plasticity increases with higher forces, as has previously been observed in stiff cells (24). However, only our data for the stiff cells but not for the soft cells seem to be in agreement with this interpretation. Our observation of a decreasing plasticity with increasing force in soft cells suggests that substantial bond rupture is already occurring at low forces and that more stable cytoskeletal structures, such as intermediate filaments, prevent further rupturing and yielding events at higher forces. This idea is also supported by our finding of a biphasic relationship between plasticity and total cell deformation (with low plasticity at both small and large cell deformations and higher plasticity at intermediate cell deformations, see Fig. S7) and by our measurements of the power-law exponent of the creep modulus, which reflects the dissipation of elastic energy, e.g., from cytoskeletal bond rupture (27). We find that the power-law exponent is only slightly increased in softer cells compared to stiffer cells even at the highest force of 16 nN.

CONCLUSIONS

In summary, hysteresis compensation eliminates the need to repeatedly de-Gauss the tweezer needle between measurements and simplifies the force calibration procedure. Most importantly, it allows for the application of arbitrary force protocols, including pyramid-like ascending and descending step forces, that are required to characterize complex cell mechanical properties, such as nonlinear time-dependent viscoelastic and plastic cell behavior, as demonstrated in this study.

SUPPORTING MATERIAL

Supporting Material can be found online at https://doi.org/10.1016/j.bpj.2020.05.018.

AUTHOR CONTRIBUTIONS

D.K.: investigation, visualization, writing: original draft preparation, and writing: review and editing. C.D.: methodology, software, investigation, visualization, and writing: original draft. W.S.: methodology. B.F.: project administration, conceptualization, methodology, writing: original draft preparation, writing: review and editing, and supervision. R.C.G.: conceptualization, formal analysis, visualization, software, writing: original draft preparation, and writing: review and editing.

ACKNOWLEDGMENTS

We thank Katharina Bick for proofreading.

This work was supported by the National Institutes of Health (HL120839) and the German Science Foundation (DFG FA336/12-1).

REFERENCES

1. Kollmannsberger, P., and B. Fabry. 2011. Linear and nonlinear rheology of living cells. *Annu. Rev. Mater. Res.* 41:75–97.
2. Bausch, A. R., F. Ziemann, …, E. Sackmann. 1998. Local measurements of viscoelastic parameters of adherent cell surfaces by magnetic bead microrheometry. *Biophys. J.* 75:2038–2049.
3. Mierke, C. T., P. Kollmannsberger, …, B. Fabry. 2010. Vinculin facilitates cell invasion into three-dimensional collagen matrices. *J. Biol. Chem.* 285:13121–13130.
4. Strick, T. R., V. Croquette, and D. Bensimon. 2000. Single-molecule analysis of DNA uncoiling by a type II topoisomerase. *Nature.* 404:901–904.
5. Neuman, K. C., T. Lionnet, and J.-F. Allemand. 2007. Single-molecule micromanipulation techniques. *Annu. Rev. Mater. Res.* 37:33–67.
6. Ashkin, A., J. M. Dziedzic, …, S. Chu. 1986. Observation of a single-beam gradient force optical trap for dielectric particles. *Opt. Lett.* 11:288–290.
7. Hunt, T. P., and R. M. Westervelt. 2006. Dielectrophoresis tweezers for single cell manipulation. *Biomed. Microdevices.* 8:227–230.
8. Fisher, J. K., L. Vicci, …, R. Superfine. 2006. Magnetic force micromanipulation systems for the biological sciences. *Nano.* 1:191–205.
9. Neuman, K. C., and A. Nagy. 2008. Single-molecule force spectroscopy: optical tweezers, magnetic tweezers and atomic force microscopy. *Nat. Methods.* 5:491–505.
10. Bessalova, V., N. Perov, and V. Rodionova. 2016. New approaches in the design of magnetic tweezers-current magnetic tweezers. *J. Magn. Magn. Mater.* 415:66–71.
11. Sarkar, R., and V. V. Rybenkov. 2016. A guide to magnetic tweezers and their applications. *Front. Physiol.* 4:48.
12. Basoli, F., S. M. Giannitelli, …, A. Rainer. 2018. Biomechanical characterization at the cell scale: present and prospects. *Front Physiol.* 9:1449.
13. Tanase, M., N. Biais, and M. Sheetz. 2007. Magnetic tweezers in cell biology. *Methods Cell Biol.* 83:473–493.
14. Kollmannsberger, P., and B. Fabry. 2007. High-force magnetic tweezers with force feedback for biological applications. *Rev. Sci. Instrum.* 78:114301.
15. Landgraf, F. J. G., M. Emura, and M. F. de Campos. 2008. On the Steinmetz hysteresis law. *J. Magn. Magn. Mater.* 320:e531–e534.
16. Randall, W. F. 1937. Nickel-iron alloys of high permeability, with special reference to mumetal. *J. Inst. Electr. Eng.* 80:647–658.
17. Trepat, X., M. Grabulosa, …, R. Farré. 2003. Oscillatory magnetic tweezers based on ferromagnetic beads and simple coaxial coils. *Rev. Sci. Instrum.* 74:4012–4020.
18. Amblard, F., B. Yurke, …, S. Leibler. 1996. A magnetic manipulator for studying local rheology and micromechanical properties of biological systems. *Rev. Sci. Instrum.* 67:818–827.
19. Bonakdar, N. 2013. Cell mechanics in response to large forces and deformations. PhD thesis (FAU Erlangen).
20. Publicover, N. G., C. G. Marsh, …, I. Chatterjee. 1999. Effects of microscope objectives on magnetic field exposures. *Bioelectromagnetics.* 20:387–395.
21. Van Rossum, G., and F. L. Drake, Jr. 1995. Python Tutorial. Centrum voor Wiskunde en Informatica, Amsterdam, The Netherlands.
22. Stuurman, N., A. Edelstein, …, R. D. Vale. 2010. Computer control of microscopes using μmanager. *Curr. Protoc. Mol. Biol.* Chapter 14:Unit14.20.
23. van der Walt, S., J. L. Schönberger, …, T. Yu; scikit-image Contributors. 2014. scikit-image: image processing in Python. *PeerJ.* 2:e453.
24. Bonakdar, N., R. Gerum, …, B. Fabry. 2016. Mechanical plasticity of cells. *Nat. Mater.* 15:1090–1094.
25. Nishizaka, T., Q. Shi, and M. P. Sheetz. 2000. Position-dependent linkages of fibronectin- integrin-cytoskeleton. *Proc. Natl. Acad. Sci. USA.* 97:692–697.
26. Hildebrandt, J. 1969. Comparison of mathematical models for cat lung and viscoelastic balloon derived by Laplace transform methods from pressure-volume data. *Bull. Math. Biophys.* 31:651–667.
27. Fabry, B., G. N. Maksym, …, J. J. Fredberg. 2001. Scaling the microrheology of living cells. *Phys. Rev. Lett.* 87:148102.
28. Kollmannsberger, P., C. T. Mierke, and B. Fabry. 2011. Nonlinear viscoelasticity of adherent cells is controlled by cytoskeletal tension. *Soft Matter.* 7:3127.
29. Wang, N., I. M. Tolić-Nørrelykke, …, D. Stamenović. 2002. Cell prestress. I. Stiffness and prestress are closely associated in adherent contractile cells. *Am. J. Physiol. Cell Physiol.* 282:C606–C616.

Biophysical Journal, Volume *119*

Supplemental Information

High-Force Magnetic Tweezers with Hysteresis-Free Force Feedback

Delf Kah, Christopher Dürrbeck, Werner Schneider, Ben Fabry, and Richard Carl Gerum

S1 SAMPLE PREPARATION FOR CALIBRATION (BEADS IN PDMS OIL)

To calibrate the magnetic tweezers, beads are suspended in polydimethylsiloxane (silicone oil) of known viscosity (Sigma-Aldrich, η = 1 to 30 Pa·s) inside a Teflon ring (inner diameter ~ 12 mm, holds about 400 µl volume), which was super-glued to a microscope glass slide (75 x 25 mm). Note that plastic slides or plastic dishes are not suitable because the electrostatic surface interacts with the beads.

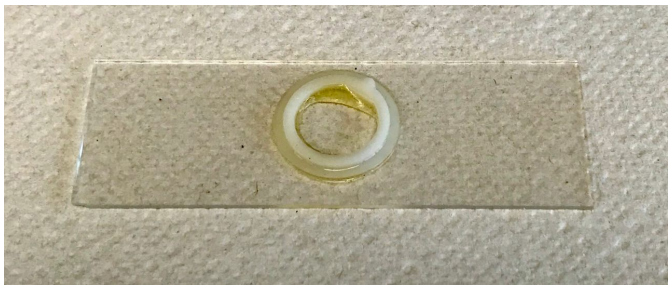

Figure S1: Specimen container for calibration measurements

The following steps are needed to prepare the sample for calibration:

- Pipette ~ 10^6 beads suspended in pure water into the Teflon ring.
- Heat the glass slide (e.g. on a heat plate) until all the water has evaporated.
- Fill the specimen holder with PDMS oil (approx. 400 µL) so that a small meniscus forms. Depending on the force range for the desired calibration, viscosities ranging from 1 to 30 Pa·s can be used.
- Mix beads and oil thoroughly with a toothpick or pipette tip. The beads should be evenly distributed throughout the PDMS.
- Place the sample in a vacuum desiccator at a pressure of ~ 10 mbar for 5–10 min to remove air bubbles created during mixing. The necessary time depends on the viscosity of the oil. For lower viscosities, shorter times are sufficient.
- The sample is ready to be placed on the microscope stage. Insert the tweezer needle, move the slide so that a bead at the same focal plane as the tweezer tip is located ~ 50 µm away from the tweezer tip, and apply the calibration protocol (alternating on and off phases (1 s each) of the magnetic field).

S2 FUNCTION FOR FITTING MULTIPLE STEPS

In the following, we describe how the data of the bead displacement versus time can be analyzed for the case of pyramidal force steps. At the beginning of each new force-up step ($t = t_{\mathrm{on}}$), a power-law response (Eq. 1, first part and Eq. 2) starts. At the beginning of each new force-down step ($t = t_{\mathrm{off}}$), a power-law response with the same viscoelastic parameters but with negative sign starts (Eq. 1 second part), while the plastic deformation remains "frozen" in time (Eq. 2) (1).

$$\begin{aligned} d_{\mathrm{viscoelastic}}(t) =& a \cdot \Delta F \cdot \left(\frac{t - t_{\mathrm{on}}}{t_{1\mathrm{s}}}\right)^{\beta} \cdot \Theta(t - t_{\mathrm{on}}) \\ & - a \cdot \Delta F \cdot \left(\frac{t - t_{\mathrm{off}}}{t_{1\mathrm{s}}}\right)^{\beta} \cdot \Theta(t - t_{\mathrm{off}}) \end{aligned} \tag{1}$$

$$d_{\mathrm{plastic}}(t) = s \cdot \Delta F \cdot \left(\frac{\min(t - t_{\mathrm{on}}, t_{\mathrm{off}} - t_{\mathrm{s}})}{t_{1\mathrm{s}}}\right)^{\beta} \cdot \Theta(t - t_{\mathrm{on}}) \tag{2}$$

$$d(t) = d_{\mathrm{viscoelastic}}(t) + d_{\mathrm{plastic}} \tag{3}$$

$\Theta(t)$ is the Heaviside step function, $\min(a, b)$ denotes the smaller value of (a, b).

S3 SEPARATION INTO A SOFT AND A STIFF COHORT

For comparing the behavior of soft cells with stiff cells, the cells are divided into a soft and a stiff cohort based on the total compliance ($a + s$) of each cell measured at a force of 1 nN.

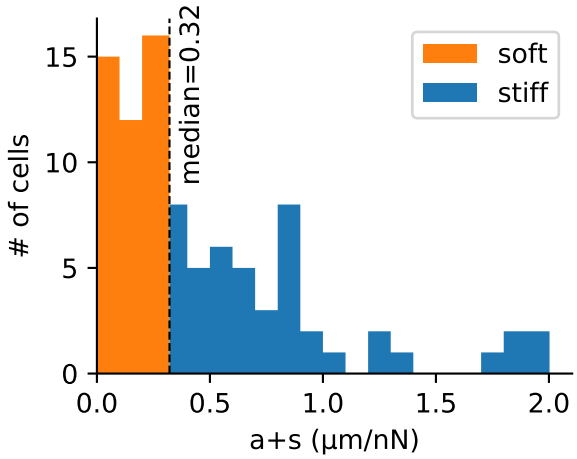

Figure S3: Histogram of the total compliance ($a + s$) of 87 cells measured at 1 nN. The median of the total compliance (0.32 µm/nN) is used to divide the cells into a soft (orange) and a stiff (blue) cohort.

S4 QUALITY OF FIT

The bead displacement in response to the applied magnetic force was fitted to a power-law as described in the section *Force Calibration*. The fit, however, gives meaningful results only if the connection between the bead and cytoskeleton remains intact during the entire measurement and if the cell does not respond actively to the applied force. Measurements for which these conditions are not met are readily identifiable by a poor fit quality and unphysical fit parameters, in particular a negative viscoelastic compliance and a power-law exponent larger than unity. Therefore, cells were included only when $a > 0$ and $\beta < 1$ for all forces. In addition, the coefficient of determination R^2 and the square root of the 98% percentile of the squared error $\sqrt{\mathrm{SE}_{98}}$ were computed for every measurement. The measurement was included only if $\sqrt{\mathrm{SE}_{98}} < 0.23\,\mu\mathrm{m}$ and $R^2 > 0.991$. Because some of the more compliant cells (displacements larger than 5 µm) occasionally show $\sqrt{\mathrm{SE}_{98}}$ errors larger than 0.23 µm, we included them if $R^2 > 0.9996$. In total, 31% of all measured cells were excluded from subsequent analysis. Appendix Figs. S4.1–S4.3 show the measured and fitted bead displacements for all included (S4.1, S4.2) and excluded (S4.3) cells.

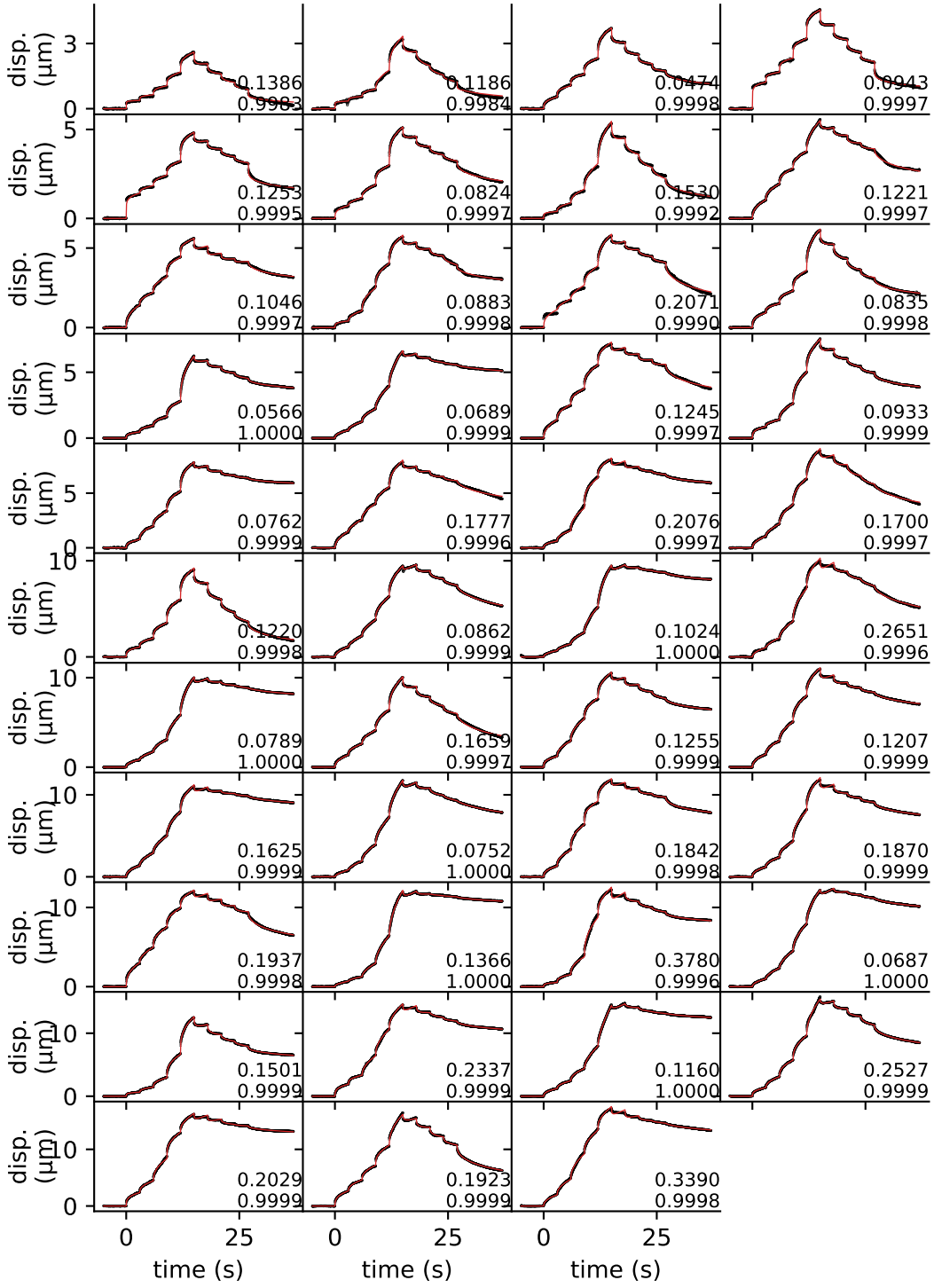

Figure S4.1: All experimental data of **stiff** fibroblasts **selected** for evaluation of the viscoelastic and plastic compliance. Black dots indicate the measured bead displacements, and red lines indicate the power-law fit. The numbers in the bottom right corner of every plot indicate the values for $\sqrt{\mathrm{SE}_{98}}$ (top) and R^2 (bottom)

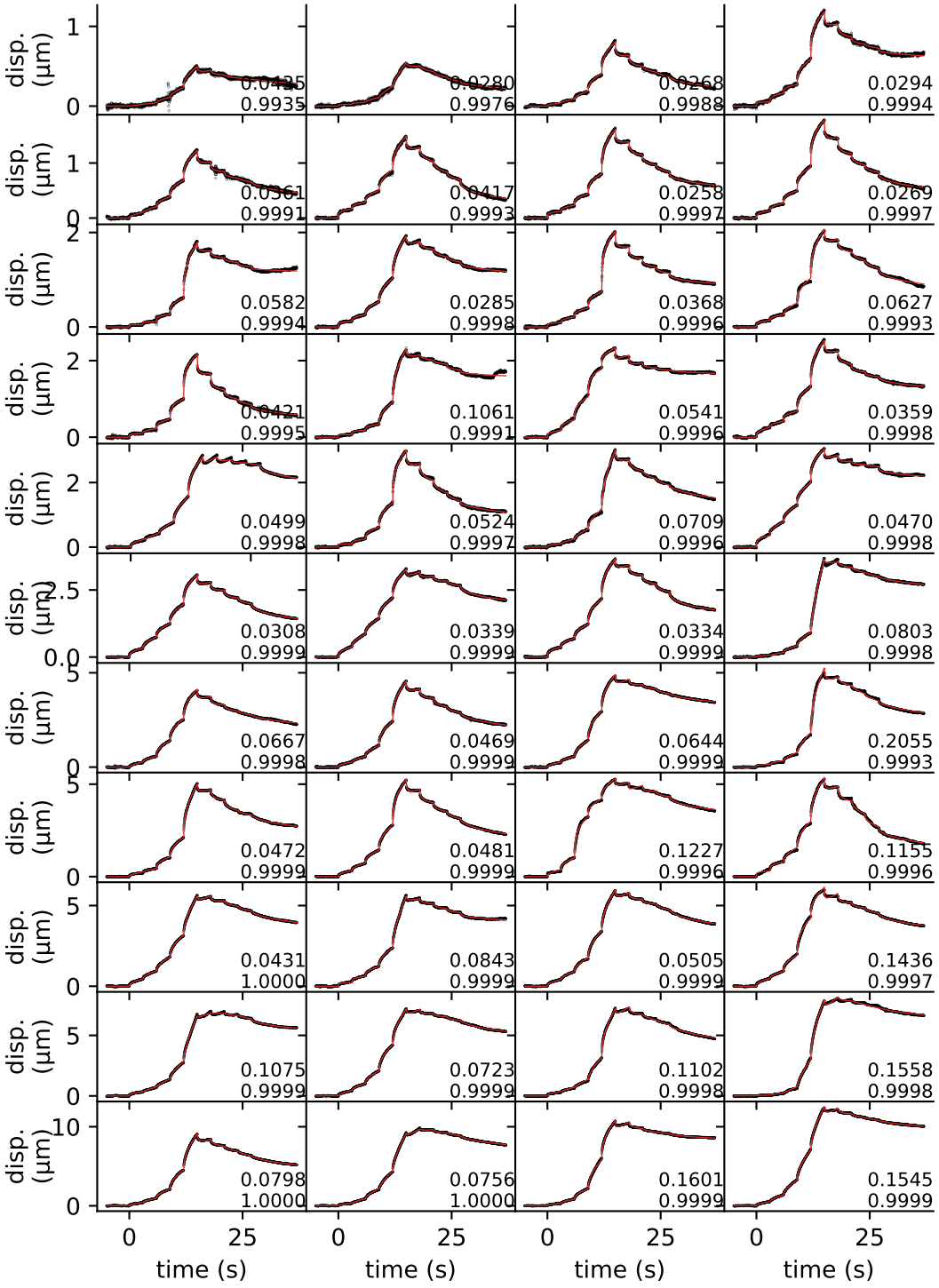

Figure S4.2: All experimental data of **soft** fibroblasts **selected** for evaluation of the viscoelastic and plastic compliance. Black dots indicate the measured bead displacements, and red lines indicate the power-law fit. The numbers in the bottom right corner of every plot indicate the values for $\sqrt{\mathrm{SE}_{98}}$ (top) and R^2 (bottom)

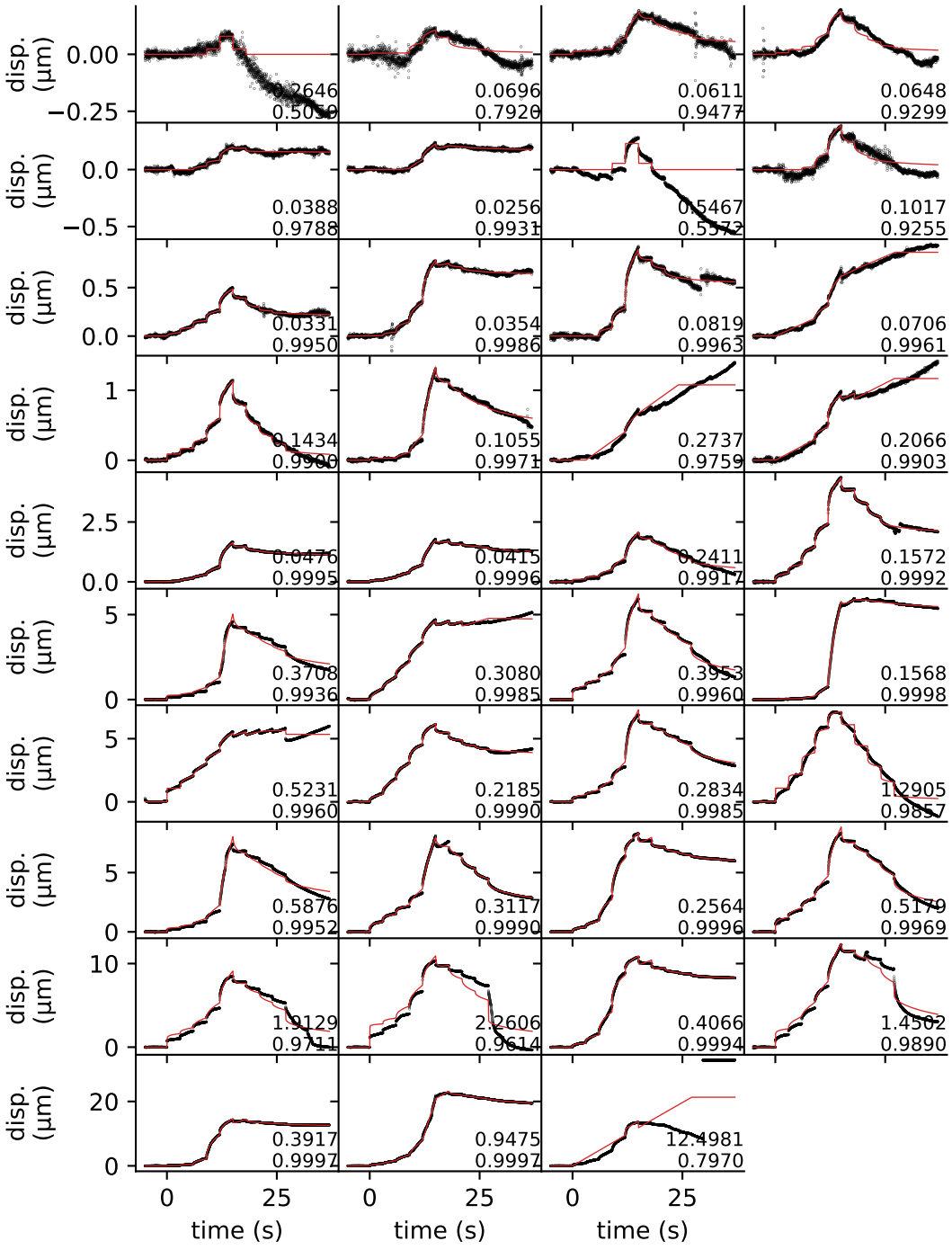

Figure S4.3: All experimental data of fibroblasts **not selected** for evaluation of the viscoelastic and plastic compliance. Black dots indicate the measured bead displacements, and red lines indicate the power-law fit. The numbers in the bottom right corner of every plot indicate the values for $\sqrt{\mathrm{SE}_{98}}$ (top) and R^2 (bottom)

S5 MAGNETIZATION OF STEEL VS. MU-METAL

To demonstrate the different magnetic properties of ST37 steel and machined (and not properly annealed) Mu-metal, magnetization curves for tweezer needles of both materials were recorded (Fig. S5). For this purpose, we applied a triangular current protocol (as described in section *Validation of hysteresis compensation*) and measured the magnetic induction. For both materials we found a pronounced hysteresis (coercivity of 1.3 mT). At a solenoid current of 2 A, the steel needle showed a maximum magnetic induction of 27.9 mT, while the Mu-metal needle reached only a value of 10.9 mT. This can be explained by a higher saturation flux density of steel compared to Mu-metal. Note that the Mu-metal needle has not been thermally annealed in a hydrogen atmosphere after sharpening the tip, which is required to restore its hysteresis-minimizing properties.

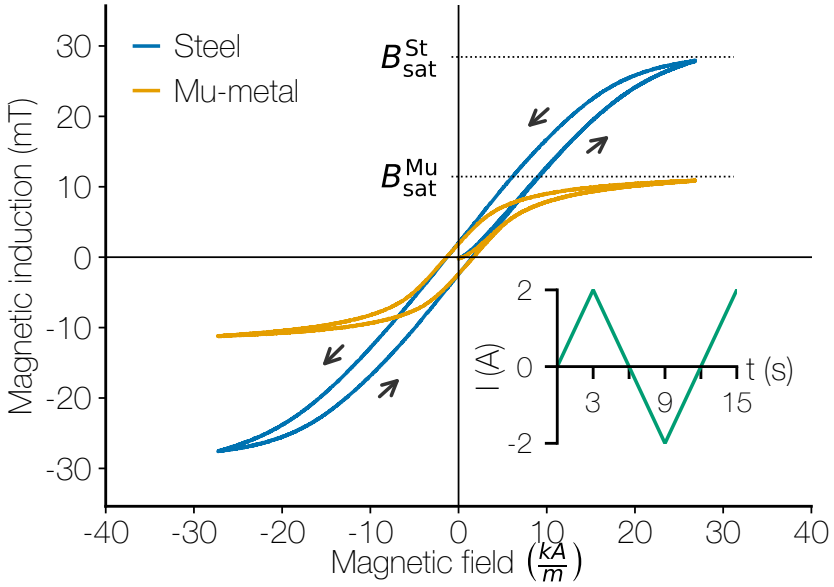

Figure S5: Magnetization curve of a tweezer needle made of ST37 steel (blue curve) and machined Mu-metal (orange curve), measured with a Hall probe. The solenoid current followed a triangular protocol (inset). The magnetic induction saturated at 27.9 mT for the steel needle and at 10.9 mT for the Mu-metal needle. Remanence and coercivity were similar for steel and Mu-metal.

S6 QUALITY OF CALIBRATION

To assess the robustness of the calibration fit, we estimated the probability distribution of the fit parameters using the Markov chain Monte Carlo (MCMC) method (2) with the Metropolis algorithm (3). With this method, we can assign for each possible tuple of fit parameters a probability p for correctly describing the measured calibration data. This probability is defined here as the product of the probabilities (taken over all data points) that the difference between the measured and the fitted force is smaller than ±5 nN. The value of 5 nN is an arbitrary choice and does not affect the shape of the probability distribution.

The metropolis algorithm starts with a parameter tuple that was estimated with a least squares fit (Table 1, main text). In each iteration, a new parameter tuple is proposed by adding a random steps to the previous parameter tuple (Gaussian distributed, with $\mu = 0$, $\sigma_{p_1} = 200$, $\sigma_{p_2} = 1$, $\sigma_{p_3} = 5$). If the probability p_{new} of this new parameter tuple is higher than the probability p_{old} of the old parameter tuple, the new parameter tuple is accepted directly. Otherwise, the new parameter tuple is accepted with a probability of $p_{\text{new}}/p_{\text{old}}$. If the new parameter tuple is rejected, the old parameter tuple is maintained.

Fig. S6.1-S6.3 shows the parameter distributions and probability fluctuations over 10^6 iterations (traces). In all configurations, the distributions of all three fit parameters follow a normal distribution. All parameter traces are uncorrelated, indicating that the chosen start parameters, the method for calculating p, and our choice for the random step sizes were reasonable.

Tab. S6 compares the mean value of all fit parameters and the standard deviation of the parameter distributions in all configurations. The standard deviation of the parameter distribution of almost all fit parameters in all configurations is less than 10 %, except for the configuration of St37 needle and Fe20 beads where the standard deviation of the parameter p_1 is slightly higher. The relative uncertainty of the fit parameters is, as expected, proportional to the force amplitude of the bead needle combination, as the higher force amplitudes show a better signal to noise ratio. The fit parameter values determined by a simple least-square-fit (see section *Force Calibration*) agree with the mean values determined by the MCMC method with a maximum deviation of 2 %.

Table S6: Summary of the Markov chain Monte Carlo evaluation of the fitting quality for the magnetic tweezer calibrations. For each fit parameter the mean value as well as the absolute and relative standard deviation of the sampled parameter distribution are shown.

core material	bead	p_1		p_2		p_3	
St37	Fe20	78.6±8.1	10.30%	0.47±0.03	5.30%	9.54±0.67	6.98%
Mu-metal	Fe80	146.6±11.0	7.46%	0.52±0.03	4.47%	10.10±0.53	5.17%
St37	Fe80	203.3±10.7	5.22%	0.70±0.02	2.79%	17.81±0.51	2.85%

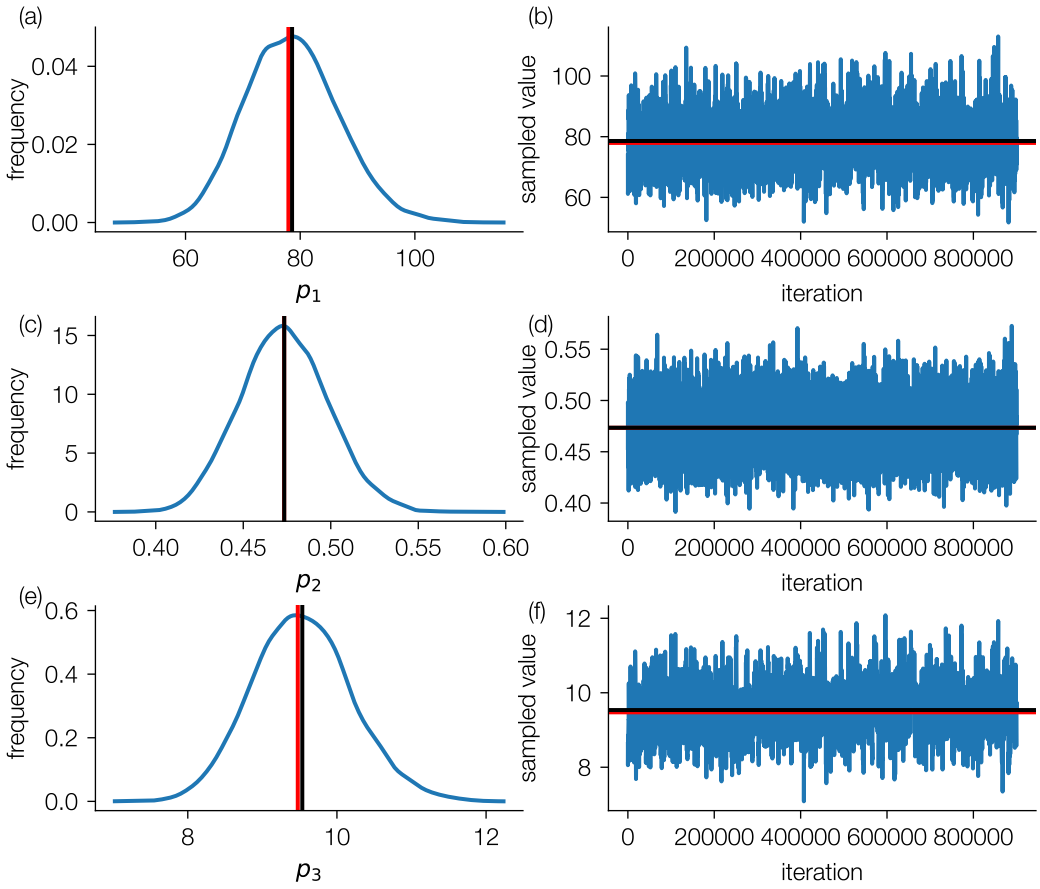

Figure S6.1: Markov chain Monte Carlo evaluation of the fitting quality for calibrations with St37 needle and Fe20 beads. (a,c,e) Kernel density estimation of the distribution of the fit parameters over 10^6 iterations. (b,d,f) Traces of the fit parameters over 10^6 iterations. Black lines indicate the mean of a single fit parameter. Red lines indicate the values from the fit parameter tuple with the single highest probability p.

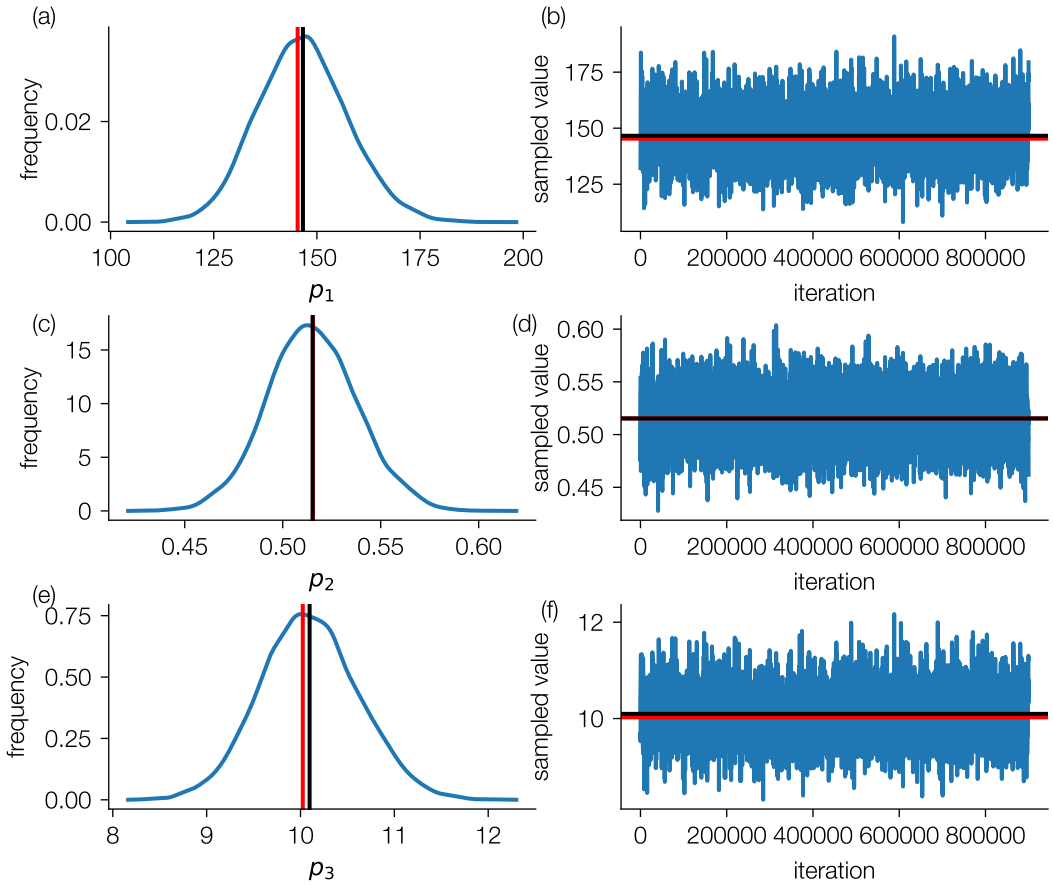

Figure S6.2: Markov chain Monte Carlo evaluation of the fitting quality for calibrations with Mu-metal needle and Fe80 beads. (a,c,e) Kernel density estimation of the distribution of the fit parameters over 10^6 iterations. (b,d,f) Traces of the fit parameters over 10^6 iterations. Black lines indicate the mean of a single fit parameter. Red lines indicate the values from the fit parameter tuple with the single highest probability p.

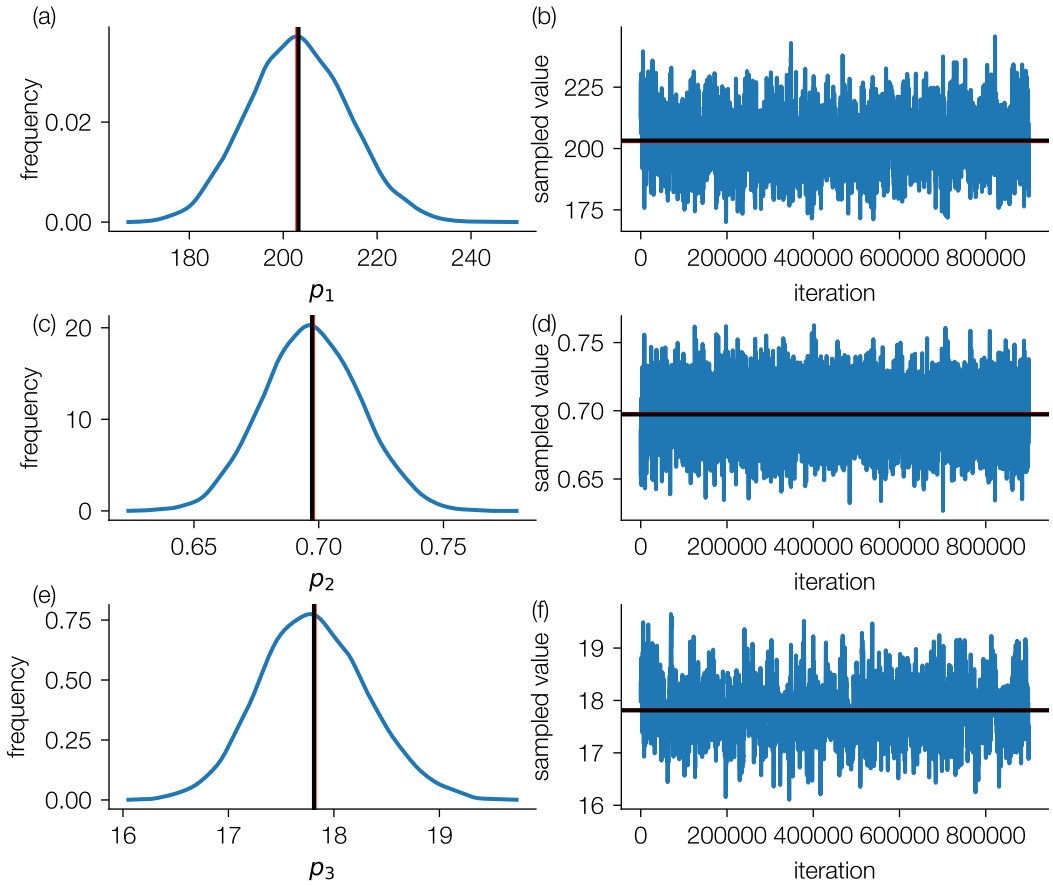

Figure S6.3: Markov chain Monte Carlo evaluation of the fitting quality for calibrations with St37 needle and Fe80 beads. (a,c,e) Kernel density estimation of the distribution of the fit parameters over 10^6 iterations. (b,d,f) Traces of the fit parameters over 10^6 iterations. Black lines indicate the mean of a single fit parameter. Red lines indicate the values from the fit parameter tuple with the single highest probability p.

S7 BI-PHASIC RESPONSE OF PLASTIC COMPLIANCE VERSUS TOTAL CELL DEFORMATION

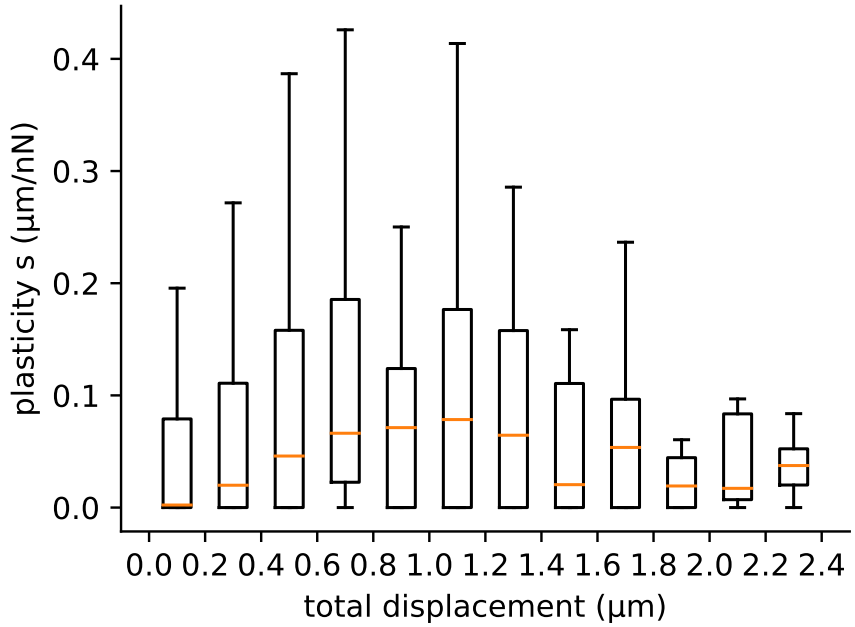

Figure S7: Plastic compliance versus total cell deformation. Plasticity data are taken from the experiment in Fig. 5 (main text) from all cells and all force steps. The plastic compliance is plotted versus the total bead displacement (binned in intervals of 200 nm) that was measured at the end of the respective force step. Boxes show median plasticity for each bin, 25%/75% percentiles, and 1.5 interquantile range.

REFERENCES

1. Bonakdar, N., R. C. Gerum, M. Kuhn, M. Spörrer, A. Lippert, W. Schneider, K. E. Aifantis, and B. Fabry, 2016. Mechanical plasticity of cells. *Nat. Mater.* 15:1090–1094. http://www.nature.com/doifinder/10.1038/nmat4689.

2. Hastings, W., 1970. Monte Carlo sampling methods using Markov chains and their applications. *Biometrika* 51:97–109. https://academic.oup.com/biomet/article-abstract/57/1/97/284580.

3. Metropolis, N., A. W. Rosenbluth, M. N. Rosenbluth, A. H. Teller, and E. Teller, 1953. Equation of state calculations by fast computing machines. *J. Chem. Phys.* 21:1087–1092. http://aip.scitation.org/doi/10.1063/1.1699114.